Highly efficient immobilized PN^{3}P-pincer iridium catalyst for dehydrogenation of neat formic acid

Lujain Alrais [a], Sandeep Suryabhan Gholap [a], Indranil Dutta [a], Edy Abou-Hamad [b], Benjamin W.J. Chen [c,*], Jia Zhang [c], Mohamed Nejib Hedhili [b], Jean-Marie Basset [a,d,**], Kuo-Wei Huang [a,e,**]

[a] *Chemistry Program, KAUST Catalysis Center and Division of Physical Science and Engineering, King Abdullah University of Science and Technology, Thuwal 23955-6900, Saudi Arabia*
[b] *Core Labs, King Abdullah University of Science and Technology, Thuwal 23955-6900, Saudi Arabia*
[c] *Institute of High-Performance Computing (IHPC), Agency for Science, Technology and Research (A*STAR) Fusionopolis Way, #16-16 Connexis, Singapore 138632, Singapore*
[d] *Ecole National Supérieure de Chimie de Paris (ENSCP), 75231 Cedex 05 Paris, France*
[e] *Institute of Materials Research and Engineering (IMRE) and Institute of Sustainability for Chemicals, Energy and Environment (ISCE2), Agency for Science, Technology and Research (A*STAR), Singapore 138634, Singapore*

ARTICLE INFO

ABSTRACT

Formic acid (FA) has been well recognized as one of the most promising hydrogen carriers. The dehydrogenation of the FA could offer an efficient process to on-demand hydrogen generation with a suitable catalyst. Homogeneous catalysts have demonstrated superior activity and selectivity compared to traditional heterogeneous catalysis. However, the latter is preferred for large-scale applications. By incorporating the homogeneous organometallic complex onto an appropriate support, the unique features of both types of catalysts can be combined and utilized effectively. Herein, we synthesized an immobilized PN^{3}P-Ir pincer catalyst (**2**) supported onto KCC-1, a 3D fibrous silica nanosphere that exhibits a high surface area and contains a tetracoordinate aluminum site. To reduce the use of volatile additives, the choice of cesium formate (CsO$_2$CH) was found to be crucial as at 80–90 °C, CsO$_2$CH could act as a reaction medium and serve as basic additive. Remarkable reactivities under neat conditions were achieved with a TOF of 13,290 h^{-1} and a TON of up to 540,000. The comparative study indicates a significant improvement of **2** from its homogenous counterpart, PN^{3}P-IrH$_3$ (**1**).

1. Introduction

Hydrogen (H$_2$) is a clean energy carrier to enable the storage and utilization of low-carbon electricity for the renewable energy future [1, 2]. Unfortunately, employing H$_2$ as an energy carrier at scale is associated with safety, storage, and transportation issues [3,4]. Over the years, different strategies have been proposed [5]. In particular, liquid hydrogen organic carriers (LHOC), such as formic acid (FA), methylcyclohexane/toluene, and methanol, hydrazine, and ammonia, have been considered potential candidates as they contain sufficient volumetric H$_2$ storage capacities compared to that in a high-pressure H$_2$ tank at 700 bar [6]. Among them, FA possesses several desirable properties

such as low toxicity, inflammability, and low dehydrogenation reaction temperature; [7] thus, its liquid nature may serve as a safe fuel alternative for fuel cell applications [7–9]. Furthermore, recent analysis suggests that FA could offer the lowest carbon-equivalent emissions [10] and may serve as one of the most affordable green energy carriers [11] when compared with other options, such as ammonia and methanol. The design of a suitable catalyst can direct the decomposition of FA, favoring the dehydrogenation pathway instead of the dehydration route [12]. The selective dehydrogenation of FA to produce H$_2$ and carbon dioxide (CO$_2$) has been extensively studied using homogenous [13–21] and heterogeneous [22–32] catalysts. Homogenous catalyst systems are known to demonstrate better activity and superior selectivity but suffer

from disadvantages in terms of catalyst separation, recovery, and short lifetime. Further, most of the reports include the use of various additives and solvents to enhance the activity. On the other hand, heterogeneous catalysts, which may be easily recovered and reused, encounter several challenges concerning selectivity, activity, and the need for different additives to achieve satisfactory production of H_2 [4]. Moreover, the development of heterogonous catalysis is hindered by the narrow knowledge of the active sites and reaction elementary steps involved in catalysis. To circumvent such issues, immobilizing catalysts onto solid support offers a straightforward strategy to combine the advantages of homogeneous complexes and heterogeneous support [33]. This can be achieved via two approaches, supported homogeneous catalysis (SHC) and surface organometallic chemistry (SOMC) [34,35]. In the SHC pathway, the design and incorporation of the organic ligand onto the support are conducted first, followed by the complexation with a metal precursor. However, in such a method, the preparation of a different ligand/support system is necessary for each new catalyst, and the resulting catalysts may not have the same activity and selectivity as their homogenous analogs due to the change in the local chemical environment [36–43]. In contrast in SOMC, homogeneous complexes are directly grafted onto the surface functionality offering an attractive strategy to immobilize organometallic species where the concepts of molecular chemistry could be transferred to heterogeneous catalysis [44]. It serves as a convenient protocol to develop new well-defined, single-site heterogeneous catalyst systems [45]. Very recently, our group reported an example of an immobilized PN^{3}P-Ru pincer catalyst for the dehydrogenation of FA with a TOF of 35,000 h^{-1} and a TON of 600,000 in the Et$_3$N/DMSO medium [46]. While a high activity and stability was achieved by this Ru-based catalyst. However, the requirement of using volatile additives and solvents may limit the applications at scale [47]. A further purification steps are necessary to remove the undesired volatile additives and solvents vapors from the gas-stream increasing the complexity and cost of system [47,48]. This led us to investigate other metal systems that are more active and avoid the utilization of volatile additives/solvents. Herein, we report the synthesis of an immobilized PN^{3}P-Ir pincer catalyst **2** supported onto tetracoordinate aluminum hydride support, [($\equiv$Si-O-Si$\equiv$)($\equiv$Si-O-)$_2$Al-H] **[Al-H]**, to facilitate FA dehydrogenation under neat conditions. An outstanding catalytic performance under neat conditions were achieved with a TOF of 13,290 h^{-1} and a TON of up to 540,000. The theoretical calculation revealed that catalyst **2** may bind stronger to HCOOH due to the Ir-H site being a stronger nucleophile resulting in a superior activity. To the best of our knowledge, it is the first ever heterogeneous system to afford such excellent reactivity, stability and selectivity under neat conditions.

2. Experimental section

The details of the relevant chemicals, and analysis methods involved in the experiment are provided in the Supporting Information.

2.1. The synthesis of the support [Al-H]

Generation of the isolated silanol groups required treatment at high temperatures under vacuum (10^{-5} mbar). So, KCC-1 (2.0 gm) was introduced to a quartz reactor, which was kept in a tubular furnace according to a previous report. The treatment was started with dehydration by heating up to 130 °C for 3 h, followed by dihydroxylation at 700 °C, for 16–20 h, with a heating gradient of 1 °C /min. After thermal treatment, titration with methyl lithium was performed using ether as a solvent. Quantification of the released methane indicates that the amount of silanol groups ($\equiv$Si-OH) is 1.8 mmol/g of KCC-1$_{700}$. The reaction of KCC-1$_{700}$ with DIBAL was carried out in a double Schlenk tube. KCC-1$_{700}$ (0.5 g) was reacted with DIBAL (1.0 equiv., 1.0 M in hexane), followed by the addition of dry n-pentane (3.0 mL) to obtain white powder. The white powder was washed with dry pentane (three times) to eliminate unreacted DIBAL. The solid product was dried under

vacuum (10^{-5} mbar) for 12 h. The obtained solid was introduced in a glass reactor (275 mL) and heated up to 400 °C (8 °C/h) for 1 h under a dynamic vacuum (10^{-5} mbar) to afford [($\equiv$Si–O–Si$\equiv$)($\equiv$Si–O–)$_2$Al–H] [49], **[Al–H]** (Fig. S1).

2.2. The synthesis of the catalyst 2

In a double Schlenk flask, **[Al-H]** (250 mg, 0.5 equiv., n [Al] = 0.35 mmol) was reacted at room temperature with PN^{3}P-IrH$_3$ complex, **1** (100 mg, n [1] = 0.17 mmol) in dry toluene (8.0 mL). After 12 h, the reaction was stopped, and the liquid phase was filtered into the second part of the double-Schlenk by inversing its position. Three washing and filtration cycles are performed, and the high vacuum line technique was used for 24 h to remove the remaining solvent. Solid product **2** was obtained and characterized using the following techniques and stored in a storage tube in the glove box.

2.3. General procedure for the dehydrogenation of FA

The formic acid dehydrogenation experiment was carried out in a two-necked round flask equipped with a reflux condenser and a magnetic stirrer at an appropriate temperature. The catalyst stock solution (FA/**1**, 21.7 mmol/ 2.0 μmol) was prepared freshly before use. The catalyst stock solution was injected through a septum into a flask containing CsO$_2$CH (various loading). While in the case of the immobilized catalyst, **2** (2.0 μmol) and CaO$_2$CH (various loading) were weighed inside the glovebox and transferred into the two-necked round flask and FA (21.7 mmol, 0.8 mL) was added via syringe. The evolution of the generated gas was observed and monitored using an ADM G6691A flowmeter simultaneously. The data was collected every 2 s on the computer by labview.

3. Results and discussion

3.1. Characterizations

Complex **2** was fully characterized by infrared spectroscopy (IR), solid-state (SS) NMR spectroscopy and dynamic nuclear polarization surface enhanced solid state (DNP SENS), X-ray photoelectron spectroscopy (XPS), and transmission electron microscopy (TEM). The immobilization of **2** was further supported by elemental analysis (Table S1 in SI) indicates a high loading of 3.1 wt% (1.3 mmol.g^{-1}) of Al and 7.2 wt% (0.37 mmol.g^{-1}) of Ir, with a Al/Ir ratio of 3.2. The C/Ir and N/Ir ratios were found to 21.1 and 2.4, respectively, in good agreement with the theoretical values of 21 and 3, respectively (See SI). Interestingly, the support could have appositive effects upon thermal treatment and exposure to air as the material maintains its characteristic structure at various conditions. However, at an elevated temperature of 250 °C the iridium hydride signal completely disappeared, and changes can be observed in the overall structural features of **2** (Figs. S2 and S3).

The **[Al-H]** support and **2** were analyzed by FT-IR (Fig. 1), revealing a signal at 3743 cm^{-1} assigned to the silanols ($\nu\equiv$Si-OH) that remain intact on the support. Additionally, a broadband signal around 3600 cm^{-1} appeared due to the formation of hydrogen bonds between compound **1** and the silanols. A weak signal was observed at 3430 cm^{-1} assigned to the ν_{N-H} arm of **1**.

The signals at 2252 cm^{-1} and 2170 cm^{-1} attributed to ($\nu_{Si-H/Si-H2}$), respectively with a noticeable decrease in intensity after grafting. At room temperature, the Si-H$_x$ could not be removed from the surface, the simplest explanation is an overlap with signals from **1**. The two series of peaks at the regions 3060–2800 cm^{-1} and 1490–1360 cm^{-1} account for the alkyl and aryl signals (ν_{C-H} and δ_{C-H}), respectively. The peak at 1942 cm^{-1} correspond to the ν_{Al-H} in agreement with the previous reported data [49], which was not observed after the immobilization reaction. Concomitantly, new bands appeared at 2120 cm^{-1} and 1997 cm^{-1} assigned to the ν_{Ir-H} signals [50]. These IR results are consistent with the
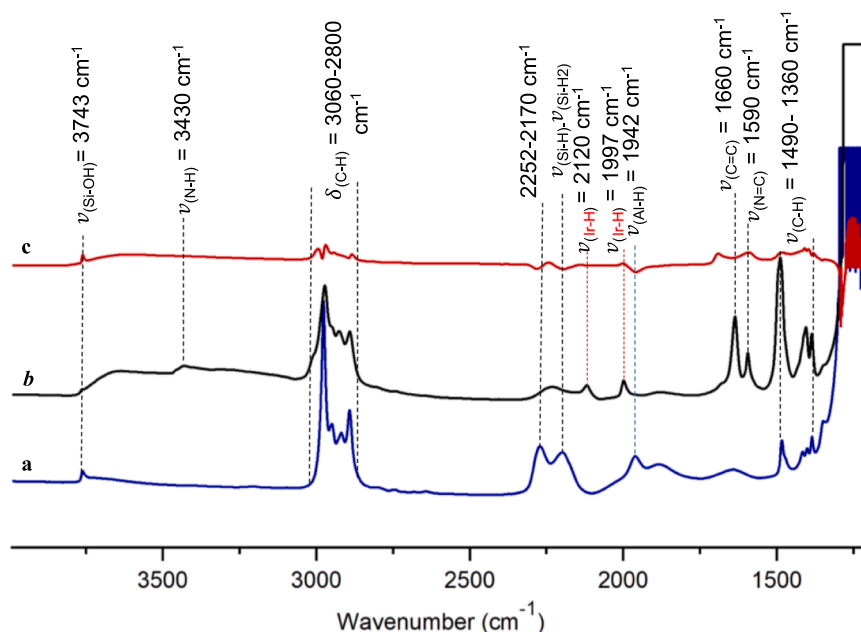
Fig. 1. FT-IR spectrum of a) [(≡Si-O-Si≡)(≡Si-O-)$_2$Al-H] **[Al-H]**, b) [(≡Si-O-Si≡)(≡Si-O-)$_2$Al-(PN^{3}P-IrH$_3$) **2**, c) Subtraction of a and b.

pre-grafted **1**, in which two signals at 1970 cm^{-1} and 2060 cm^{-1} are attributed to the Ir-hydrides [51] (Fig. 2). As a result of bonding to the electrophilic Al-H species, the shift of the Ir-hydrides peaks from 1970 cm^{-1} and 2060 cm^{-1} to 2120 and 1997 cm^{-1} in the supported catalyst **2** was observed. Insight into the coordination sphere of **2** was obtained using advanced solid-state NMR. To enhance sensitivity for surface species, dynamic nuclear polarization surface-enhanced solid-state (DNP SENS) NMR spectrometry was employed. The ^{1}H NMR spectra (Fig. 3) show an intense peak at δ 0.9 ppm corresponding to the ^{t}Bu [P-C-(C**H**$_3$)$_3$] group of **1**, and the ^{i}Bu [Si-C**H**$_2$-CH-(C**H**$_3$)$_2$] group of **[Al-H]** support. The signal at δ 4.4 ppm is assigned to Si-**H**, Si-**H**$_2$ of support, and N-**H** of **1**. The peak at δ 6.8 ppm corresponds to aromatic protons, while the signal at δ − 26.6 ppm corresponds to Ir-H. Therefore, based on the data, we can reasonably infer that the formation of **2** (as shown in Scheme 1) is well represented. Further evidence was provided by the ^{15}N SENS-DNP NMR spectroscopy, where three
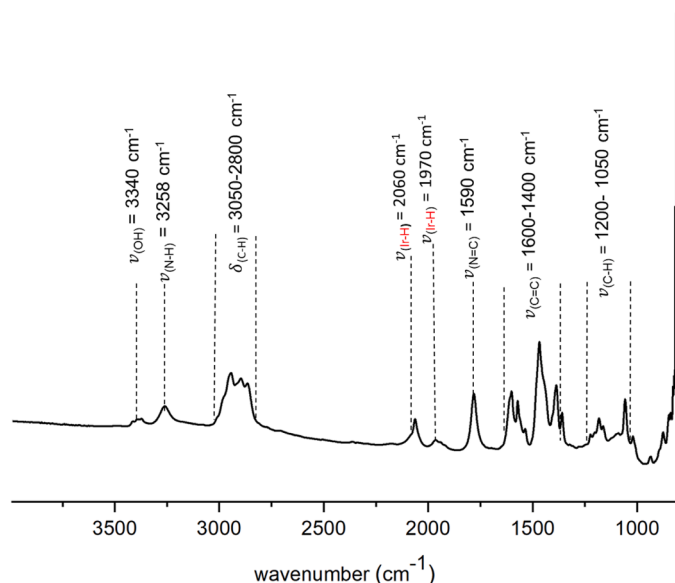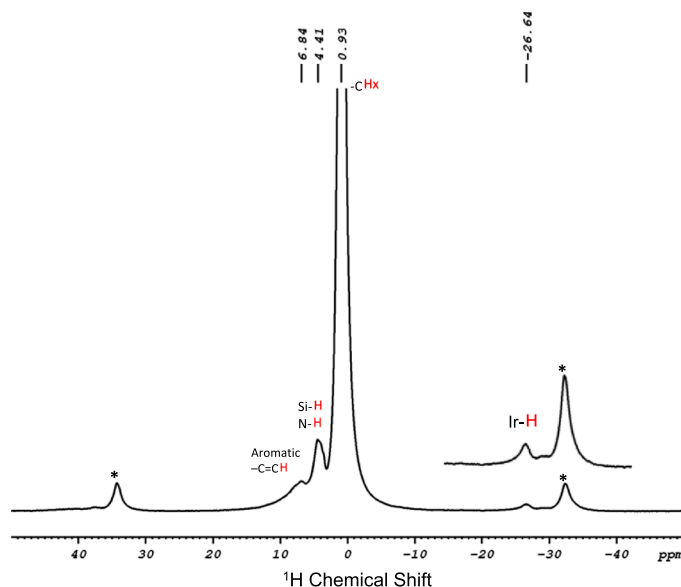

Fig. 3. ^{1}H MAS solid-state NMR spectrum of **2**.

distinguished signals of N atoms from different chemical environments were observed, in contrast to **1** (Fig. 4). The ^{13}C CP/MAS NMR and ^{31}P NMR of **2** showed consistent values, indicating that the pincer complex was retained after grafting (Figs. S4 and S5).

The interpretation from 2D spectra revealed autocorrelations in double-quantum (DQ) and triple-quantum (TQ) frequencies. A strong autocorrelation peak was observed at δ 0.9 ppm in both DQ and TQ spectra and appeared at δ 1.7 and 2.6 ppm in the ω1 dimensions respectively, which correspond to methyl protons of ^{t}Bu group in **2** (Figs. S6 and S7) supporting the complete immobilization of the complex **1** onto the **[Al-H]** support.

The chemical status of the element was studied with the high-resolution XPS. The spectra of **2** revealed the presence of Ir^{III}, indicated by the two signals at 61.3 eV and 64.5 eV, which align with those observed in catalyst **1** suggesting a similar chemical environment (Figs. S9 and S10) [52]. The elemental mapping of Ir and Al using

Fig. 2. FT-IR spectrum of **1** before grafting.
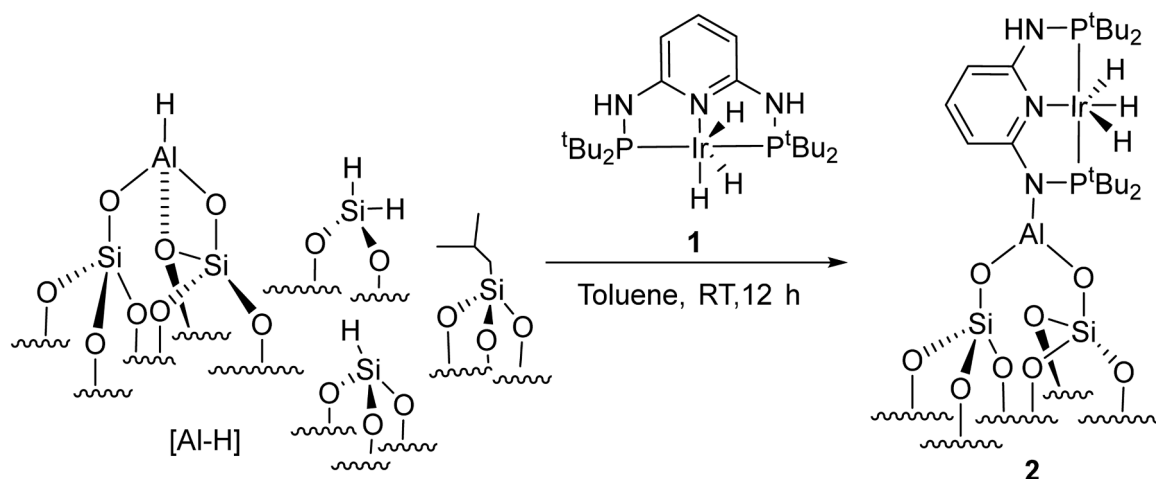
Scheme 1. Synthesis of Immobilized PN^{3}P-Ir Pincer Complex 2.
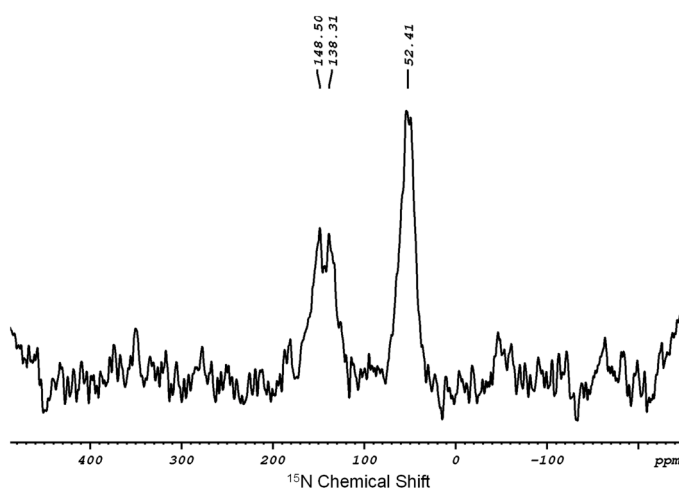
Fig. 4. ^{15}N DNP SENS NMR spectrum of **2**.

STEM-EDS imaging technique demonstrate a well and uniform distribution throughout the entire structure, highlighting an advantageous feature of the fibrous 3D KCC-1 material. This feature provides accessible sites for metals to bind and creates more accessible active sites for catalysis (Fig. 5).

3.2. Formic acid dehydrogenation reaction

The catalytic performance of **2** and **1** were examined for the dehydrogenation of FA. Initially, we evaluated the activity of **1** in the presence of Et$_3$N in DMSO giving an initial TOF of 22,380 h^{-1} (see SI, Table S2, entry 1). To our delight, under similar conditions, catalyst **2** provided a higher TOF of 43,000 h^{-1} (see SI, Table S2, entry 2) showing higher efficiency of the heterogeneous system compared to **1**. These remarkable results inspired us to investigate the catalytic efficiency of **2** under neat and solvent-free conditions. In the absence of solvent, lower TOF was obtained (see SI, Table S2, entry 3). The effect of solid bases as an additive during the catalytic reaction was further investigated. Alkali metal salts (potassium formate and sodium formate) are commonly used additives to dehydrogenate FA.[53,54] Their nonvolatile nature makes them advantageous compared to amine-based additives. However, the employment of such additives in solvent-free/neat conditions is mostly ineffective, and there is only one report available in the literature [48].

Preliminary results suggested that in the presence of either NaO$_2$CH or KO$_2$CH, the dehydrogenation of FA was slow and resulted in only low

conversion(see SI, Table S3, entries 1 and 2). Subsequently, the reaction was performed in the presence of catalyst **2** with CsO$_2$CH. Initially, the reaction rate was slow, however, as it proceeds, a maximum TOF up to 930 h^{-1} with 45% conversion was obtained (see SI, Table S3, entry 3). To understand the role of support, a control reaction with only support was conducted. This resulted in only 4% conversion, suggesting the importance of metal center during catalytic FA dehydrogenation (See SI, Table S3, entry 4). These observations prompted us to optimize the amount of CsO$_2$CH in the reaction (see SI table S3, entries 5–11). We examined various ratios of FA/CsO$_2$CH, and the ratio (8:1) achieved a 99% conversion with a higher TOF of up to 13,290 h^{-1} and immediate gas release (see SI table S3, entry 10). Upon completion of the batch reaction, recharging with a fresh amount of FA resumed gas production. This process was repeated 15 times, resulting in conversions ranging from 99% to 94%, yielding a total of 12.9 L of gas and a TON of 133,943. Between each run, catalyst **2** was exposed to atmospheric conditions, which may affect its efficiency (see SI, Table S5). Furthermore, optimization with a higher FA/CsO$_2$CH ratio afforded an incomplete conversion with lower TOF values (see SI table S3, entries 5–9). Under similar reaction conditions, we studied the catalytic performance of **1** and achieved 91% conversion and maximum TOF up to 5700 h^{-1} was observed (see SI table S4, entry 7). These comparable studies suggested that **2** exhibits more prominent reactivity than complex **1**. The analyses of the produced gases from the reaction mixture were confirmed by gas chromatography showing the production of only H$_2$ and CO$_2$, and no CO was detected under the TCD-GC limit of 15 ppm (see Figs. S14 and S15). These observations suggest a good potential for fuel cell applications where CO poisoning of electrodes must be prevented. To gain more information about the effect of formic acid concentration on reaction rate, reactions with 91% and 95% FA concentrations were performed under the same optimized condition and it was found that the reaction was faster in the case of 91% FA (Figs. S19). To gain an insight into the catalytic activity and durability of **1** and **2**, an optimized catalytic performance study was conducted in which a syringe pump was used to keep a constant rate of addition of FA over a period of time. In the case of **1**, a TON up to 260,000 was observed over 100 h with 25.4 L of gas collected (Fig. 6A). Similarly, the optimized catalytic performance of **2** afforded a TON up to 540,000 over a period of approximately 250 h and 51 L of gas was recorded (Fig. 6B). We speculated that the choice of cesium formate (CsO$_2$CH) as an additive may be crucial due to its low melting point of 50 °C. Consequently, in general, in FA dehydrogenation conditions, at the temperature of 80–90 °C, CsO$_2$CH may function as a reaction medium and a basic additive to facilitate the dehydrogenation reaction.

In order to understand the mechanism, a controlled experiment was conducted in which **2** were reacted with an excess amount of FA for 1 h.
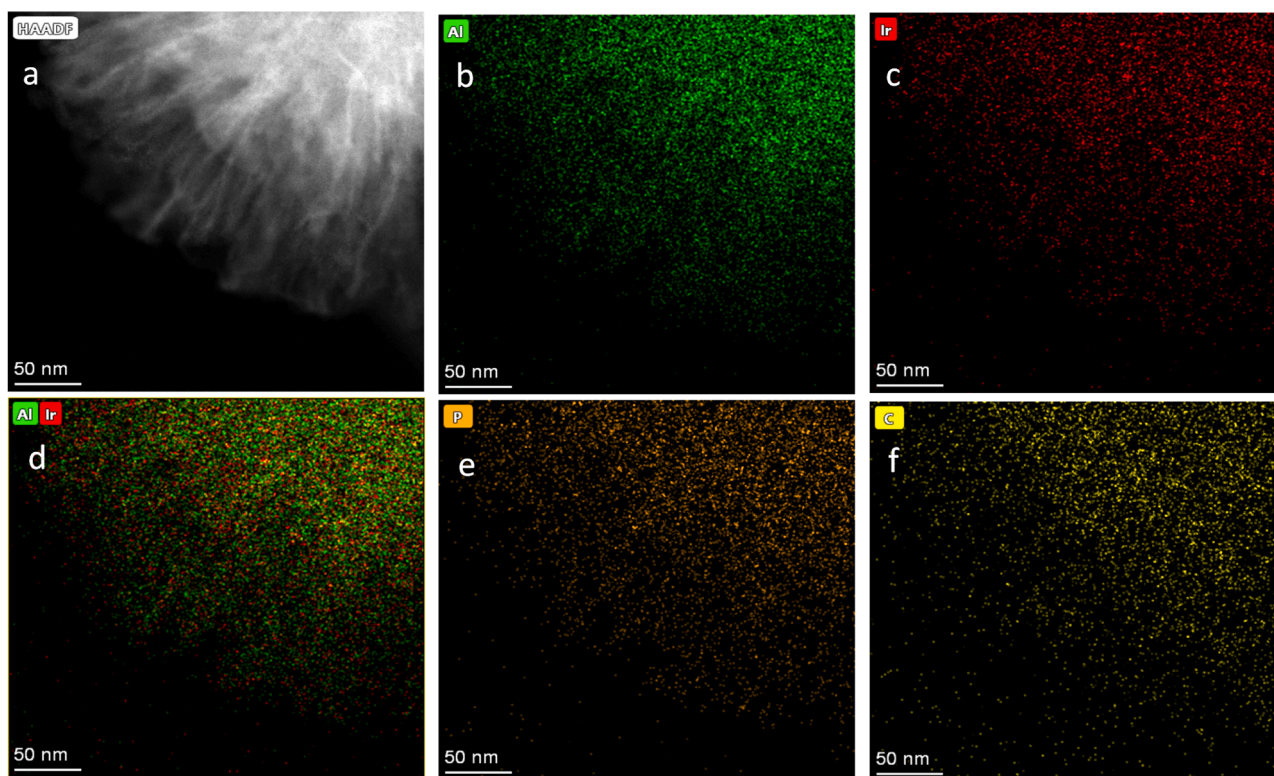
Fig. 5. HAADF-STEM (a) images and elemental mapping of Aluminum (b), iridium (c), aluminum and iridium (d), phosphorus (e), and carbon (f).
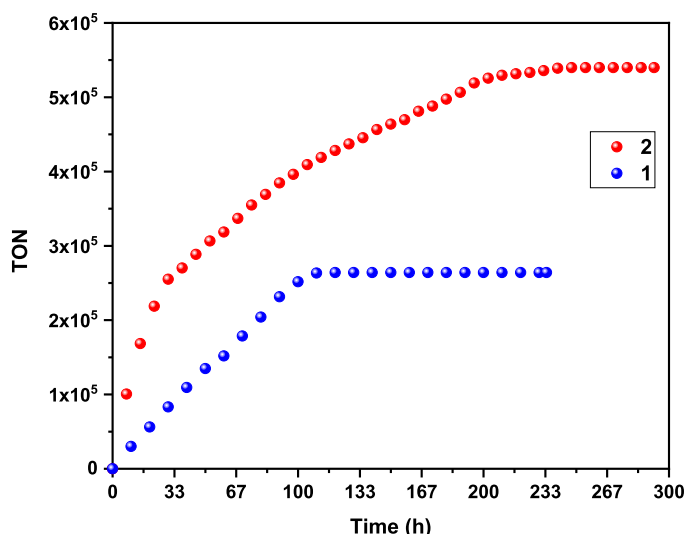

Fig. 6. 1) Continuous flow reaction of catalyst **1**. 2) Continuous flow reaction of catalyst **2**.

Later the resulting material was washed with dry pentane to remove the residual FA, followed by drying under a high vacuum. The ^{1}H solid-state NMR spectra revealed an additional peak at δ 8.2 ppm, (Fig. 7) corresponding to the coordination of the formate, while the rest of the peaks were similar to those observed in catalyst **2**. Moreover, ^{13}C MAS NMR spectra indicated the presence of a formate peak at δ 173 ppm (Fig. S8). Based on these results, a probable mechanism was proposed involving the coordination of the formic acid to an Ir center with the concurrent release of H_2 gas to generate intermediate **2`**. Subsequently, the release of CO_2 gas completes the catalytic cycle (Fig. S22). Further information was provided by FT-IR of the reaction mixture at different stages of the

dehydrogenation (see SI for details). The spectrum shows a broad band at the range of 3100–3800 cm^{-1} because of the support saturation upon exposure to cesium formate and FA. The two series of peaks at the regions 3000–2500 cm^{-1} and 1440–1340 cm^{-1} account for the alkyl and aryl signals (ν_{C-H} and δ_{C-H}), respectively. The spectra recorded at room temperature contains a signature at 2344 cm^{-1}, assigned to CO_2 which decreased after the reaction temperature was increased to 90 °C. It was not conclusive if the CO_2 moiety is coordinated to the PN^{3}P-Ir complex or the support. The peaks in 1975 and 2090 cm^{-1} correspond to the ν_{Ir-Hx}, which may indicate to the change in the Ir-H_x modes during the reaction. The C-O and C=O fragments of the formate appeared in 1735 and 1680 cm^{-1} (Fig. S23).

4. DFT calculation

In the attempt to rationalize the activity of **2** for FA decomposition, we performed first-principles periodic density functional theory (DFT) calculations. Following our previous work [46], the single-site tetra-coordinate aluminum hydride support **[Al-H]** was modeled as an amorphous silica surface with an OH density of 1.69 nm^{-2} [55,56]. The immobilized catalyst **2** was modeled by the adsorption of **1** onto **[Al-H]** (Fig. 8a); a water molecule was additionally adsorbed on Al to saturate the Al center since water is always present in commercially available FA (a more detailed discussion of the model selection for catalyst **2** is presented in Section S5, Fig. S24).

We then probed the decomposition of FA over **1** and **2** with the explicit assistance of two water molecules (Fig. 8b). Without water, the barriers for the reaction of FA over **1** were significantly higher (Fig. S25), suggesting that hydrogen bonding and shuttling play important roles in FA decomposition over the catalysts in this study, consistent with our experiments showing an increase in catalyst activity with higher amounts of water (as discussed above) and as also observed in other works.[57–59] We considered only the formate (HCOO*) pathway and not the carboxyl (COOH*) pathway as COOH* is known to be a precursor for CO production [60], but no CO was produced by
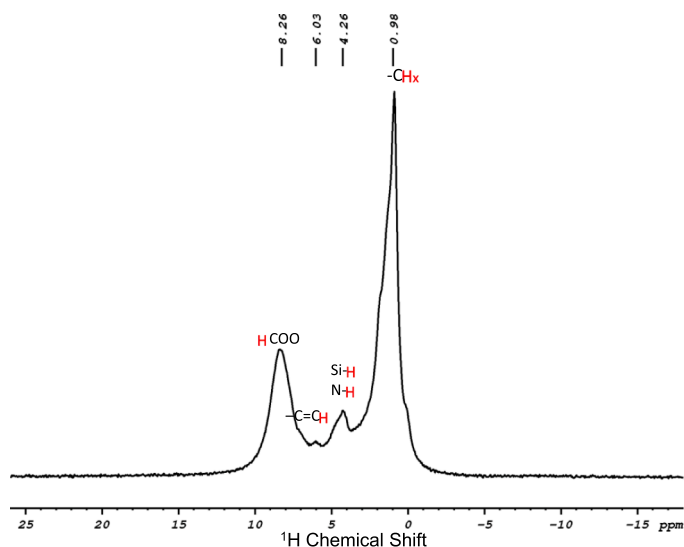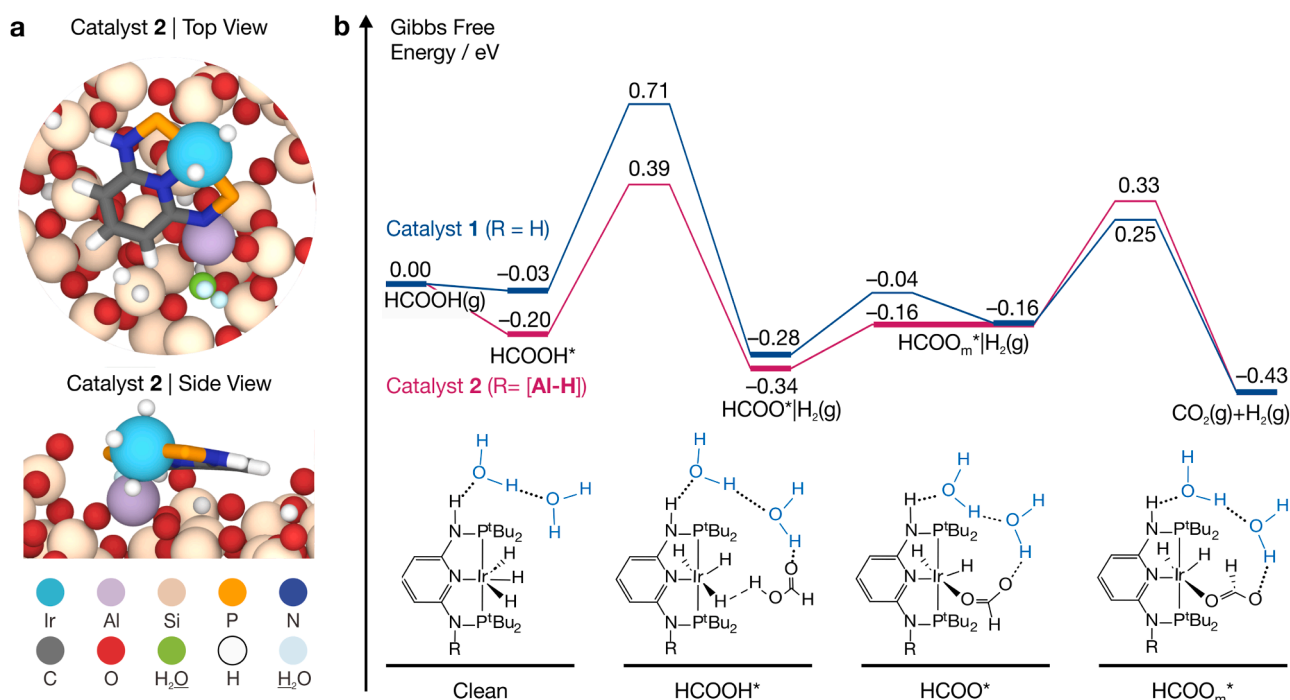
Fig. 7. ^{1}H NMR spectra of the intermediate **2`**.

Fig. 8. First-principles DFT modeling of FA decomposition over catalysts **1** and **2**. (a) Top and side views of the atomistic models for grafted catalyst **2**. Butyl groups are omitted from the figure and the PN^{3}P pincer ligand is depicted as sticks for clarity. (b) Potential energy diagrams for the reaction of FA over catalysts **1** and **2**. Energies are Gibbs free energies relative to the initial states. Illustrations of catalytic intermediates are shown at the bottom, with H_2O highlighted in light blue. Atomistic structures of each of the intermediates are provided in Figs. S26 and S27 for catalysts **1** and **2**, respectively.

either **1** or **2** (shown in the gas analysis). For both catalysts **1** and **2**, the most favorable reaction mechanism involves the following: in the first elementary step, HCOOH adsorbs onto the catalysts via a non-covalent interaction between the –OH group of HCOOH and the axial H ligand. The subsequent reaction of HCOOH* with the axial H ligand, akin to an acid-base reaction, leads to the release of H_2 and the formation of HCOO* . On both catalysts **1** and **2**, HCOO* is the most stable adsorbed intermediate, consistent with the observation of formate in the ^{13}C CP/MAS NMR spectra after drying the spent catalyst (Fig. S8). In the next step, HCOO* then flips to form HCOOm* where the C–H bond points downwards and is closer to the active Ir center, priming it for its decomposition, which finally releases CO$\neg_2$ and restores the H ligand to

the Ir center.

The energetic span for FA decomposition over **2** is 0.67 eV, lower than the energetic span of 0.74 eV over **1** (Fig. 8b). This is consistent with the higher activity of grafted catalyst **2**. The lower energetic span of catalyst **2** can be attributed mainly to its ability to stabilize HCOOH* (by 0.17 eV) and the HCOOH* →HCOO* transition state (by 0.32 eV) (Fig. 8b), as compared with catalyst **1**. To understand this, we performed charge density difference analyses, which revealed a build-up of electron density between the –OH group of HCOOH* and the axial H ligand (Fig. S28). A Bader charge analysis further showed that catalyst **2** possesses a total charge of –0.75 |e| (Ir center and ligands only; excluding Al and the support), as compared with a charge of –0.43 |e| ¬for the

analogous portion of catalyst **1** (i.e., excluding *a* H of one N–H group). The larger negative charge on the grafted catalyst increases the nucleophilic nature of the axial H ligand, which may strengthen its non-covalent interaction with HCOOH* and thereby stabilize the HCOOH* →HCOO* transition state. Supporting our hypothesis, calculations using catalyst **1** with a total system charge of −1 showed stronger binding of HCOOH* and reduced HCOOH* →HCOO* barriers as compared with catalyst **1** with no charge (Table S6). The larger negative charge on catalyst **2** is therefore likely the main reason for its improved FA decomposition activity.

5. Conclusion

In conclusion, a highly efficient neat FA dehydrogenation system catalyzed by **1** and **2** has been described. Both catalysts demonstrate excellent performance in a solvent-free environment, exhibiting high TOF and TON. Results indicate a significant activity enhancement and longer lifetime in the case of **2**, which can be attributed to the surface rigidity creating an isolated site and preventing undesired bimolecular deactivation. The data presented here exemplify how the "Catalysis by Design" concept leads to new and improved catalysts. Therefore, the introduction of a strong Lewis acid center (Al site) between the silica surface and the active catalytic site remarkably alters the performance of an Iridium catalyst **2**. The theoretical data disclose the superior activity of **2** by the larger negative charge compared to **1**. CsO_2CH may also play a crucial role as a basic additive that could activate the catalyst in addition to serving as a reaction medium to mediate FA dehydrogenation.

CRediT authorship contribution statement

Lujain Alrais: Experimental Measurements, Data Analysis, Manuscript Preparation. **Sandeep Suryabhan Gholap**: Experimental Measurements, Data Analysis, review & editing. **Indranil Dutta:** Experimental Measurements, Data Analysis, review & editing. **Benjamin W. J. Chen:** DFT calculation, Writing – review. **Jia Zhang**: DFT calculation, Writing – review. **Mohamed Nejib Hedhili**: XPS measurement. **Edy Abou-Hamad**: NMR-analysis. **Jean-Marie Basset**: review & editing, Supervision. **Kuo-Wei Huang**: Conceptualization, Writing – review & editing, Supervision, Project administration.

Declaration of Competing Interest

The authors declare that they have no known competing financial interests or personal relationships that could have appeared to influence the work reported in this paper**.**

Data Availability

Data will be made available on request.

Appendix A. Supporting information

Supplementary data associated with this article can be found in the online version at doi:10.1016/j.apcatb.2023.123439.

References

[1] A. Turner John, Sustainable hydrogen production, Science 305 (2004) 972–974.
[2] M. Whitesides George, W. Crabtree George, Don't forget long-term fundamental research in energy, Science 315 (2007) 796–798.
[3] N. Armaroli, V. Balzani, The hydrogen issue, ChemSusChem 4 (2011) 21–36.
[4] I. Dutta, S. Chatterjee, H. Cheng, R.K. Parsapur, Z. Liu, Z. Li, E. Ye, H. Kawanami, J. S.C. Low, Z. Lai, X.J. Loh, K.-W. Huang, Formic acid to power towards low-carbon economy, Adv. Energy Mater. 12 (2022) 2103799.
[5] J.O.M. Bockris, The hydrogen economy: its history, Int. J. Hydrogen Energy 38 (2013) 2579–2588.
[6] M. Niermann, A. Beckendorff, M. Kaltschmitt, K. Bonhoff, Liquid organic hydrogen carrier (LOHC) – assessment based on chemical and economic properties, Int. J. Hydrogen Energy 44 (2019) 6631–6654.
[7] J. Eppinger, K.-W. Huang, Formic acid as a hydrogen energy carrier, ACS Energy Lett. 2 (2017) 188–195.
[8] K. Mazloomi, C. Gomes, Hydrogen as an energy carrier: prospects and challenges, Renew. Sust. Energ. Rev. 16 (2012) 3024–3033.
[9] M. Grasemann, G. Laurenczy, Formic acid as a hydrogen source – recent developments and future trends, Energy Environ. Sci. 5 (2012) 8171–8181.
[10] I. Dutta, R.K. Parsapur, S. Chatterjee, A.M. Hengne, D. Tan, K. Peramaiah, T. I. Solling, O.J. Nielsen, K.-W. Huang, The role of fugitive hydrogen emissions in selecting hydrogen carriers, ACS Energy Lett. 8 (2023) 3251–3257.
[11] B.S. Crandall, T. Brix, R.S. Weber, F. Jiao, Techno-economic assessment of green H_2 carrier supply chains, Energy Fuels 37 (2023) 1441–1450.
[12] K. Sordakis, C. Tang, L.K. Vogt, H. Junge, P.J. Dyson, M. Beller, G. Laurenczy, Homogeneous catalysis for sustainable hydrogen storage in formic acid and alcohols, Chem. Rev. 118 (2018) 372–433.
[13] A. Boddien, B. Loges, H. Junge, M. Beller, Hydrogen generation at ambient conditions: application in fuel cells, ChemSusChem 1 (2008) 751–758.
[14] S. Fukuzumi, T. Kobayashi, T. Suenobu, Unusually large tunneling effect on highly efficient generation of hydrogen and hydrogen isotopes in pH-selective decomposition of formic acid catalyzed by a heterodinuclear iridium−ruthenium complex in water, J. Am. Chem. Soc. 132 (2010) 1496–1497.
[15] J.F. Hull, Y. Himeda, W.-H. Wang, B. Hashiguchi, R. Periana, D.J. Szalda, J. T. Muckerman, E. Fujita, Reversible hydrogen storage using CO_2 and a proton-switchable iridium catalyst in aqueous media under mild temperatures and pressures, Nat. Chem. 4 (2012) 383–388.
[16] E. Fujita, J.T. Muckerman, Y. Himeda, Interconversion of CO_2 and formic acid by bio-inspired Ir complexes with pendent bases, Biochim. Biophys. Acta 2013 (1827) 1031–1038.
[17] W. Gan, D.J.M. Snelders, P.J. Dyson, G. Laurenczy, Ruthenium(II)-catalyzed hydrogen generation from formic acid using cationic, ammoniomethyl-substituted triarylphosphine ligands, ChemCatChem 5 (2013) 1126–1132.
[18] M. Czaun, A. Goeppert, J. Kothandaraman, R.B. May, R. Haiges, G.K.S. Prakash, G. A. Olah, Formic acid as a hydrogen storage medium: ruthenium-catalyzed generation of hydrogen from formic acid in emulsions, ACS Catal. 4 (2014) 311–320.
[19] G.A. Filonenko, R. vanPutten, E.N. Schulpen, E.J.M. Hensen, E.A. Pidko, Highly efficient reversible hydrogenation of carbon dioxide to formates using a ruthenium PNP-pincer catalyst, ChemCatChem 6 (2014) 1526–1530.
[20] A. Matsunami, Y. Kayaki, T. Ikariya, Enhanced hydrogen generation from formic acid by half-sandwich iridium(III) complexes with metal/NH bifunctionality: a pronounced switch from transfer hydrogenation, Eur. J. Chem. 21 (2015) 13513–13517.
[21] Y. Pan, C.-L. Pan, Y. Zhang, H. Li, S. Min, X. Guo, B. Zheng, H. Chen, A. Anders, Z. Lai, J. Zheng, K.-W. Huang, Selective hydrogen generation from formic acid with well-defined complexes of ruthenium and phosphorus–nitrogen PN3-pincer Ligand, Chem. Asian J. 11 (2016) 1357–1360.
[22] X. Zhou, Y. Huang, W. Xing, C. Liu, J. Liao, T. Lu, High-quality hydrogen from the catalyzed decomposition of formic acid by Pd–Au/C and Pd–Ag/C, Chem. Commun. (2008) 3540–3542.
[23] Y. Huang, X. Zhou, M. Yin, C. Liu, W. Xing, Novel PdAu@Au/C core−shell catalyst: superior activity and selectivity in formic acid decomposition for hydrogen generation, Chem. Mater. 22 (2010) 5122–5128.
[24] K. Tedsree, T. Li, S. Jones, C.W.A. Chan, K.M.K. Yu, P.A.J. Bagot, E.A. Marquis, G. D.W. Smith, S.C.E. Tsang, Hydrogen production from formic acid decomposition at room temperature using a Ag–Pd core–shell nanocatalyst, Nat. Nanotechnol. 6 (2011) 302–307.
[25] X. Gu, Z.-H. Lu, H.-L. Jiang, T. Akita, Q. Xu, Synergistic catalysis of metal–organic framework-immobilized Au–Pd nanoparticles in dehydrogenation of formic acid for chemical hydrogen storage, J. Am. Chem. Soc. 133 (2011) 11822–11825.
[26] Q.-Y. Bi, X.-L. Du, Y.-M. Liu, Y. Cao, H.-Y. He, K.-N. Fan, Efficient subnanometric gold-catalyzed hydrogen generation via formic acid decomposition under ambient conditions, J. Am. Chem. Soc. 134 (2012) 8926–8933.
[27] Z.-L. Wang, J.-M. Yan, Y. Ping, H.-L. Wang, W.-T. Zheng, Q. Jiang, An efficient CoAuPd/C catalyst for hydrogen generation from formic acid at room temperature, Angew. Chem. Int. Ed. 52 (2013) 4406–4409.
[28] Q.-L. Zhu, N. Tsumori, Q. Xu, Sodium hydroxide-assisted growth of uniform Pd nanoparticles on nanoporous carbon MSC-30 for efficient and complete dehydrogenation of formic acid under ambient conditions, Chem. Sci. 5 (2014) 195–199.
[29] Z. Zheng, T. Tachikawa, T. Majima, Plasmon-enhanced formic acid dehydrogenation using anisotropic Pd–Au nanorods studied at the single-particle level, J. Am. Chem. Soc. 137 (2015) 948–957.

[30] M. Zacharska, A.L. Chuvilin, V.V. Kriventsov, S. Beloshapkin, M. Estrada, A. Simakov, D.A. Bulushev, Support effect for nanosized Au catalysts in hydrogen production from formic acid decomposition, Catal. Sci. Technol. 6 (2016) 6853–6860.

[31] T. Wang, F. Li, H. An, W. Xue, Y. Wang, Enhanced catalytic activity over palladium supported on ZrO$_2$@C with NaOH-assisted reduction for decomposition of formic acid, RSC Adv. 9 (2019) 3359–3366.

[32] Z. Wang, S. Liang, X. Meng, S. Mao, X. Lian, Y. Wang, Ultrasmall PdAu alloy nanoparticles anchored on amine-functionalized hierarchically porous carbon as additive-free catalysts for highly efficient dehydrogenation of formic acid, Appl. Catal. B: Environ. 291 (2021), 120140.

[33] C. Copéret, M. Chabanas, R. Petroff Saint-Arroman, J.-M. Basset, Homogeneous and heterogeneous catalysis: bridging the gap through surface organometallic chemistry, Angew. Chem. Int. Ed. 42 (2003) 156–181.

[34] C. Copéret, F. Allouche, K.W. Chan, M.P. Conley, M.F. Delley, A. Fedorov, I. B. Moroz, V. Mougel, M. Pucino, K. Searles, K. Yamamoto, P.A. Zhizhko, Bridging the gap between industrial and well-defined supported catalysts catalysts, Angew. Chem. Int. Ed. 57 (2018) 6398–6440.

[35] Y.R. de Miguel, Supported catalysts and their applications in synthetic organic chemistry, J. Chem. Soc. Perkin Trans. 1 (2000) 4213–4221.

[36] G.H. Gunasekar, H. Kim, S. Yoon, Dehydrogenation of formic acid using molecular Rh and Ir catalysts immobilized on bipyridine-based covalent triazine frameworks, Sustain. Energy Fuels 3 (2019) 1042–1047.

[37] C. Broicher, S.R. Foit, M. Rose, P.J.C. Hausoul, R. Palkovits, A bipyridine-based conjugated microporous polymer for the Ir-catalyzed dehydrogenation of formic acid, ACS Catal. 7 (2017) 8413–8419.

[38] D.A. Bulushev, Progress in catalytic hydrogen production from formic acid over supported metal complexes, Energies 14 (2021) 1334.

[39] W. Gan, P.J. Dyson, G. Laurenczy, Heterogeneous silica-supported ruthenium phosphine catalysts for selective formic acid decomposition, ChemCatChem 5 (2013) 3124–3130.

[40] A.V. Bavykina, M.G. Goesten, F. Kapteijn, M. Makkee, J. Gascon, Efficient production of hydrogen from formic acid using a Covalent Triazine Framework supported molecular catalyst, ChemSusChem 8 (2015) 809–812.

[41] X. Yang, E.A.P. Ling, C. Guan, Q. Zhang, W. Wu, P. Liu, N. Zheng, D. Zhang, S. Lopatin, Z. Lai, K.-W. Huang, Single-site ruthenium pincer complex knitted into porous organic polymers for dehydrogenation of formic acid, ChemSusChem 11 (2018) 3591–3598.

[42] L. Tensi, A.V. Yakimov, C. Trotta, C. Domestici, J. De Jesus Silva, S.R. Docherty, C. Zuccaccia, C. Copéret, A. Macchioni, Single-Site Iridium Picolinamide Catalyst Immobilized onto Silica for the Hydrogenation of CO$_2$ and the Dehydrogenation of Formic Acid, Inorg. Chem. 61 (2022) 10575–10586.

[43] W. Gan, P.J. Dyson, G. Laurenczy, Hydrogen storage and delivery: immobilization of a highly active homogeneous catalyst for the decomposition of formic acid to hydrogen and carbon dioxide, React. Kinet. Catal. Lett. 98 (2009) 205–213.

[44] M.K. Samantaray, E. Pump, A. Bendjeriou-Sedjerari, V. D'Elia, J.D.A. Pelletier, M. Guidotti, R. Psaro, J.-M. Basset, Surface organometallic chemistry in heterogeneous catalysis, Chem. Soc. Rev. 47 (2018) 8403–8437.

[45] J.D.A. Pelletier, J.-M. Basset, Catalysis by design: well-defined single-site heterogeneous catalysts, Acc. Chem. Res. 49 (2016) 664–677.

[46] L. Yaacoub, I. Dutta, B. Werghi, B.W.J. Chen, J. Zhang, E.A. Hamad, E.P. Ling Ang, E. Pump, A.B. Sedjerari, K.-W. Huang, J.-M. Basset, Formic acid dehydrogenation via an active ruthenium pincer catalyst immobilized on tetra-coordinated aluminum hydride species supported on fibrous silica nanospheres, ACS Catal. 12 (2022) 14408–14417.

[47] S. Kar, M. Rauch, G. Leitus, Y. Ben-David, D. Milstein, Highly efficient additive-free dehydrogenation of neat formic acid, Nat. Catal. 4 (2021) 193–201.

[48] J.J.A. Celaje, Z. Lu, E.A. Kedzie, N.J. Terrile, J.N. Lo, T.J. Williams, A prolific catalyst for dehydrogenation of neat formic acid, Nat. Commun. 7 (2016) 11308.

[49] B. Werghi, A. Bendjeriou-Sedjerari, A. Jedidi, E. Abou-Hamad, L. Cavallo, J.-M. Basset, Single-Site tetracoordinated aluminum hydride supported on mesoporous silica. from dream to reality!, Organometallics 35 (2016) 3288–3294.

[50] M. Rimoldi, D. Fodor, J.A. van Bokhoven, A. Mezzetti, A stable 16-electron iridium (iii) hydride complex grafted on SBA-15: a single-site catalyst for alkene hydrogenation, Chem. Commun. 49 (2013) 11314–11316.

[51] H.D. Empsall, E.M. Hyde, E. Mentzer, B.L. Shaw, M.F. Uttely, Some iridium hydride and tetrahydroborate complexes with bulky tertiary phosphine ligands, J. Chem. Soc. Dalton Trans. (1976) 2069–2074.

[52] H.D. Empsall, L. Zeng, M. Jia, Z. Li, Z. Lin, Y. Song, Y. Zhou, J. Cheng, C. Wang, W. Lin, Molecular Iridium complexes in metal–organic frameworks catalyze CO$_2$ hydrogenation via concerted proton and hydride transfer, J. Am. Chem. Soc. 139 (2017) 17747–17750.

[53] C. Guan, Y. Pan, T. Zhang, M.J. Ajitha, K.W. Huang, An update on formic acid dehydrogenation by homogeneous catalysis, Chem. Asian J. 15 (2020) 937–946.

[54] L. Jia, D.A. Bulushev, S. Beloshapkin, J.R.H. Ross, Hydrogen production from formic acid vapour over a Pd/C catalyst promoted by potassium salts: evidence for participation of buffer-like solution in the pores of the catalyst, Appl. Catal. B: Environ. 160–161 (2014) 35–43.

[55] C.S. Ewing, G. Bhavsar, G. Veser, J.J. McCarthy, J.K. Johnson, Accurate amorphous silica surface models from first-principles thermodynamics of surface dehydroxylation, Langmuir 30 (2014) 5133–5141.

[56] L. Li, C.S. Ewing, M. Abdelgaid, S. Banerjee, R.B. Garza, R. Hacku, N.D. Hess, S. Hong, M. Islamov, L.L. Luciani, S. Papadopoulos, C. Parker, R.A. Patel, R. Pawar, M.H. Poklar, M. Salem, F. Shabnam, P.B. Shukla, S.K. Vena, H. Wang, R. Wang, X. Wei, F. Yang, J.K. Johnson, Binding of CO and O on low-symmetry Pt clusters supported on amorphous, Silica, J. Phys. Chem. C 125 (2021) 13780–13787.

[57] B.W.J. Chen, M. Mavrikakis, Formic acid: a hydrogen-bonding cocatalyst for formate decomposition, ACS Catal. 10 (2020) 10812–10825.

[58] B.W.J. Chen, S. Bhandari, M. Mavrikakis, Role of hydrogen-bonded bimolecular formic acid–formate complexes for formic acid decomposition on copper: a combined first-principles and microkinetic modeling study, ACS Catal. 11 (2021) 4349–4361.

[59] Y. Zhang, X. Chen, B. Zheng, X. Guo, Y. Pan, H. Chen, H. Li, S. Min, C. Guan, K.-W. Huang, J. Zheng, Structural analysis of transient reaction intermediate in formic acid dehydrogenation catalysis using two-dimensional IR spectroscopy, Proc. Natl. Acad. Sci. USA 115 (2018) 12395–12400.

[60] S. Bhandari, S. Rangarajan, C.T. Maravelias, J.A. Dumesic, M. Mavrikakis, Reaction mechanism of vapor-phase formic acid decomposition over platinum catalysts: DFT, reaction kinetics experiments, and microkinetic modeling, ACS Catal. 10 (2020) 4112–4126.